Wind Energy

WILEY

RESEARCH ARTICLE OPEN ACCESS

Implementation and Validation of a Generalized Actuator Disk Parameterization for Wind Turbine Simulations Within the FastEddy Model

M. Sanchez Gomez[1] | D. Muñoz-Esparza[2] | J. A. Sauer[2]

[1]National Wind Technology Center, National Renewable Energy Laboratory, Golden, Colorado, USA | [2]Research Applications Laboratory, National Center for Atmospheric Research, Boulder, Colorado, USA

Correspondence: M. Sanchez Gomez (miguel.sanchezgomez@nrel.gov)

Received: 7 March 2024 | **Revised:** 11 June 2024 | **Accepted:** 24 June 2024

Funding: The authors want to express their greatest gratitude to Dr. Branko Kosović and Prof. Julie K. Lundquist for technical insights and facilitating this collaborative research effort. The authors would also like to thank Dr. Paula Doubrawa for providing the experimental data for the three SWiFT benchmarks and the modeling data for the code-to-code comparison. This work was authored in part by the National Renewable Energy Laboratory, operated by Alliance for Sustainable Energy, LLC, for the US Department of Energy (DOE) under Contract No. DE-AC36-08GO28308. Funding is provided by the US Department of Energy Office of Energy Efficiency and Renewable Energy Wind Energy Technologies Office. The views expressed in the article do not necessarily represent the views of the DOE or the US Government. The US Government retains and the publisher, by accepting the article for publication, acknowledges that the US Government retains a nonexclusive, paid-up, irrevocable, worldwide license to publish or reproduce the published form of this work, or allow others to do so, for US Government purposes. Contributions from DME and JAS were funded by the 2022 NCAR Research Applications Laboratory (RAL) Opportunity Award: "Wind Energy Solutions with FastEddy®." The authors would like to acknowledge high-performance computing support from Casper/Cheyenne (doi:10.5065/D6RX99HX) and Derecho (doi:10.5065/qx9a-pg09) provided by NCAR's Computational and Information Systems Laboratory (CISL), sponsored by the National Science Foundation.

Keywords: atmospheric boundary layer | large-eddy simulations | wind turbine modeling

ABSTRACT

Fast and accurate large-eddy simulation (LES) of the atmospheric boundary layer plays a crucial role in advancing wind energy research. Long-duration wind farm studies at turbine-resolving scales have become increasingly important to understand the intricate interactions between large wind farms and the atmospheric boundary layer. However, the prohibitive computational cost of these turbulence- and turbine-resolving simulations has precluded such modeling to be exercised on a regular basis. To that end, we implement and validate the generalized actuator disk (GAD) model in the computationally efficient, graphics processing unit (GPU)–resident, LES model FastEddy. We perform single-turbine simulations under three atmospheric stabilities (neutral, unstable, and stable) and compare them against observations from the Scaled Wind Farm Technology (SWiFT) facility and other LES codes from the recent Wakebench turbine wake model benchmark. Our idealized LES results agree well with observed wake velocity deficit and downstream recovery across stability regimes. Turbine response in terms of rotational speed, generated power, torque, and thrust coefficient are well predicted across stability regimes and are consistent with the LES results from the benchmark. The FastEddy simulations are found to be at least two orders of magnitude more efficient than the traditional CPU-based LES models, opening the door for realistic LES simulations of full wind plants as a viable standard practice.

1 | Introduction

The large-eddy simulation (LES) technique provides an accurate methodology for explicitly modeling the most energetic eddies in atmospheric boundary layer flows [1] and, therefore, plays a crucial role in the field of wind energy. Turbulence-resolving simulations allow for accurate modeling of wind turbine wake dynamics (e.g., [2]), predicting loads on their structural components (e.g., [3, 4]), and understanding their interaction with the atmosphere (e.g., [5–7]). However, understanding farm-to-farm interactions, for example, requires domains that span tens of kilometers along the horizontal directions at small grid spacings capable of resolving the effect of wind turbines and turbulence in the near-surface region. This type of LES modeling framework requires substantial computational resources, often making it prohibitive for real-time applications or for large-scale and/or long-duration studies.

Recently, performance and efficiency advantages have been demonstrated leveraging graphics processing units (GPUs) in lieu of traditional central processing units (CPUs) for running LES models (e.g., [8, 9]). The FastEddy model (hereafter FastEddy), introduced by Sauer and Muñoz-Esparza [10] and Muñoz-Esparza et al. [11], was developed in the Research Applications Laboratory of the National Center for Atmospheric Research (NCAR) with the intent of enabling faster and more computationally feasible turbulence-resolving LES of the atmospheric boundary layer. FastEddy exploits the characteristics of GPU hardware amenable to fine-grained parallelism including high-bandwidth memory and thousands of processing cores organized in groups capable of concurrent (parallel) processing. FastEddy has been enhanced to allow coupling to mesoscale models, proving a computationally affordable tool with novel advanced capability to perform efficient and skillful real-world simulations of atmospheric phenomena (e.g., [12–14]).

The effects of wind turbines on the flow are typically parameterized in LES codes given that resolving the entire flow field around a wind turbine blade is still too costly from a computational point of view. The simplest approach is the actuator disk model, which applies a uniform aerodynamic force perpendicular to the turbine rotor [15]. A more accurate turbine parameterization is the generalized actuator disk (GAD) model, which combines blade-element momentum theory with the actuator disk model [16]. In the GAD model, lift and drag forces are calculated based on the aerodynamic characteristics of the blade and distributed over the rotor to provide an accurate approximation for turbine thrust and rotation. In an actuator line model, rather than representing the turbine as a disk, each turbine blade is represented as a line enabling an even more realistic localized approximation of forces between turbine blades and the flow field [17].

To enable the application of FastEddy towards emerging wind energy modeling needs, we incorporate a GAD wind turbine parameterization for use in performant turbulence-resolving simulations. This development will permit numerical experiments to explore the effects of operating wind turbines under a broad range of realistic multi-scale (spanning tens of kilometers to meters) atmospheric boundary layer conditions. In particular, massively parallel, GPU-resident LES model, FastEddy, with a GAD extension can be employed to generate ensembles of wind turbine and wind farm flows, simulate farm-to-farm interactions over large regions, carry-out virtual experiments to evaluate sensitivities to modeling and turbine/farm design configurations, and generally achieve cost effective transformational advances in the state-of-the art for coupled atmosphere and turbine/farm modeling.

Here, we describe and validate an implementation of the GAD model in FastEddy. Specifically, we compare idealized, single-turbine FastEddy simulations with the GAD against observations and other LES codes for neutral, unstable, and stable atmospheric boundary layers, corresponding to the wake-model benchmark study of Doubrawa et al. [18]. The remainder of this paper is structured as follows. We provide an overview of the dataset used for validating the GAD model in FastEddy in Section 2. Section 3 describes the modeling framework and stability cases used to validate the GAD model. In Section 4, we compare the wake velocity distributions and turbine performance from FastEddy against observations and other LES codes from the benchmark study. Finally, Section 5 provides conclusions and future work. Appendix A provides and overview of the GAD model and its implementation in FastEddy.

2 | Validation Dataset

We use observational data from the Scaled Wind Farm Technology (SWiFT) facility [19] to validate the GAD implementation in FastEddy. The SWiFT facility, located in Lubbock, Texas, is surrounded by relatively flat terrain. Radiative forcing is the main driver for changes in atmospheric stability at this site [20]. Wind turbine performance and wake measurements at this site are available between 2016 and 2017, making the SWiFT facility an ideal location for validating numerical simulations of wind turbines in realistic atmospheric boundary layer flows [18, 21].

The SWiFT facility is equipped with three horizontal-axis wind turbines, a nacelle-mounted lidar, and a meteorological tower. The wind turbine at SWiFT considered here is a modified version of the 300-kW Vestas V27 with a 27-m rotor diameter D and hub height z_h at 32.1 m above the surface. Inflow atmospheric conditions to the V27 turbine are measured using a 60-m-tall meteorological tower located $2.5D$ upstream along the predominant wind direction. The met-tower is equipped with sonic anemometers at $z = 10$, 18, 32, 45, and 58 m, spanning the turbine rotor layer. Surface-layer stability is characterized using pressure, temperature, and humidity sensors near the surface ($z = 2$ m) and wind speed from the sonic anemometer at 10 m. The spatial evolution of the wake as it propagates downstream of the turbine is observed using a rear-facing, nacelle-mounted DTU SpinnerLidar [22].

We consider three simulation scenarios based on the SWiFT benchmarks [20]. The main atmospheric characteristics of each scenario are summarized in Table 1. Each benchmark is primarily defined by distinct atmospheric stability regimes, quantified using the Obukhov length $L = -u_*^3\theta/\kappa g\overline{w'\theta'}$, where u_* is the friction velocity, θ is the near-surface potential temperature, $\kappa = 0.4$ is the von Kármán constant, $g = 9.81$ m s^{-2} is the gravitational acceleration, and $\overline{w'\theta'}$ is the near-surface kinematic heat flux. The atmospheric state for each benchmark is defined

by the ensemble mean of time-averaged values observed during disparate 10-min periods at the SWiFT site. The first case, a near-neutral surface layer, is defined from six 10-min transitional periods: five 10-min periods 0.2–1.3 h before sunset and one 10-min period 2.3 h after sunrise. The second case, a weakly unstable surface layer, is from five 10-min periods during daytime conditions (1.2–2 h after sunrise). The third benchmark case is a stably stratified surface layer with low-turbulence conditions observed during six 10-min nighttime periods (between 5.3 and 6.5 h after sunset). Wake measurements from the SpinnerLidar were performed over the downstream distance from $x/D = 2$ to $x/D = 5$ in $1D$ increments for the stable and neutral atmospheric conditions. For the unstable case, wake measurements were performed only at $x/D = 3$. Generator power, torque, and rotational speed for the V27 turbine are averaged in 10-min time windows while the remaining downstream wind turbines are shut down.

Several combinations of LES codes with turbine parameterizations were compared to this SWiFT dataset as part of the International Energy Agency Wind Task 31 [23], also known as WakeBench. We include simulation results from EllipSys3D [24, 25], PALM [26], NaluWind [27, 28], WRF [21, 29], and SOWFA [30] to compare the performance of the GAD in FastEddy against other LES codes. Note that not all models provided results for all stability cases. Furthermore, wind turbines in EllipSys3D, PALM, NaluWind, and SOWFA are parameterized using an actuator line parameterization, while WRF-LES wind turbines are parameterized using the GAD.

3 | Modeling Framework

Atmospheric forcing conditions corresponding to the three stability cases described in Section 2 develop in a precursor, coarser-resolution LES with periodic boundary conditions. The neutral and unstable simulations are initialized with a constant potential temperature $\theta = 300$ K from the surface up to 1000 m, a capping inversion with $\partial\theta/\partial z = 0.08$ K m^{-1} between 1000 and 1300 m, and $\partial\theta/\partial z = 0.003$ K m^{-1} above 1300 m. The stable case is initialized with a constant potential temperature $\theta = 300$ K from the surface up to 200 m, a capping inversion with $\partial\theta/\partial z = 0.08$ K m^{-1} between 200 and 300 m, and $\partial\theta/\partial z = 0.003$ K m^{-1} above 300 m. We vary atmospheric stability by changing the surface forcing. A 0.023 K m s^{-1} kinematic heat flux and -0.5 K h^{-1} cooling rate are prescribed at the surface for the unstable and stable conditions, respectively. Spin-up time varies for each stability case. A fully developed neutral, unstable, and stable boundary layer establishes after 10, 15, and 9.1 h, respectively. Forcing conditions and domain characteristics for the neutral, unstable, and stable cases are listed in Table 2. Note that the horizontal Δx and vertical Δz_s grid spacing vary to properly resolve turbulence characteristics under the different stability conditions.

All precursor simulations are initialized with a dry atmosphere and zero latent heat flux. Time integration is performed using a third-order accurate Runge-Kutta scheme. A fifth-order upwinding advection scheme is used to discretize the advection term. The Lilly subgrid scale (SGS) model [31, 32] with a prognostic equation for SGS turbulence kinetic energy (TKE) is included. Monin-Obukov similarity theory [33] is used to approximate momentum and heat fluxes in the first grid cell above ground. Coriolis effects are included for a latitude of 33.60795° N, representative of the geographical location of the SWiFT facility. We also include Rayleigh damping in the uppermost 300 m of the domain.

A finer grid is used to better resolve the wake evolution downstream of the 27-m-diameter wind turbine. This higher resolution turbine-inclusive LES domain is initialized and forced at the lateral boundaries using the horizontally averaged one-dimensional vertical profiles of all prognostic equations (i.e., density, velocity components, potential temperature, and SGS TKE) from the precursor LES after spin-up. We rotate the wind vector to align the wind direction at hub height with the x-coordinate in the higher resolution domain, while maintaining the influence of the Coriolis terms for the SWiFT latitude. Each stability case is run for 1 h to flush the initial condition and allow turbulence to become established across the entire domain. To evaluate the effect of the GAD on the flow, we perform two sets of simulations for each stability case, one with and one without the turbine in the domain. Domain characteristics for the fine LES domain are shown in Table 3. For

TABLE 1 | Atmospheric conditions defining each benchmark at the SWiFT facility [20].

Case	$\overline{U}_h$ (m s^{-1})	$\overline{k}_h$ (m^2 s^{-2})	L (m)	$\overline{w'\theta'}$ (K m s^{-1})
Neutral	8.7	0.873	2500	−0.002
Unstable	6.7	0.687	−112	0.023
Stable	4.8	0.029	8.7	−0.005

Note: Hub-height observations of wind speed $\overline{U}_h$ and turbulence kinetic energy $\overline{k}_h$ from the upstream tower ($z_h = 32.1$ m). The near-surface Obukhov length L and kinematic heat flux $\overline{w'\theta'}$ are derived from high-frequency wind speed and temperature measurements at 10 and 2 m, respectively.

TABLE 2 | Simulation setup for the precursor LES domain for each stability case, including the horizontal grid spacing Δx, vertical grid spacing near the surface Δz_s, initial uniform vertical grid spacing in domain before stretching is applied $\langle \Delta z \rangle$, number of grid points along each i-coordinate n_i, time step Δt, geostrophic wind forcing U_g, V_g, inversion layer height z_i, roughness length z_0, surface kinematic heat flux $\overline{w'\theta}$, and surface cooling rate $\dot{T}$.

Case	Δx (m)	Δz_s, $\langle \Delta z \rangle$ (m)	(n_x, n_y, n_z) (—)	Δt (s)	U_g, V_g (m s^{-1})	z_i (m)	z_0 (m)	$\overline{w'\theta'}_s$ (K m s^{-1})	$\dot{T}_s$ (K h^{-1})
Neutral	10	6.8, 10	(304, 202, 154)	0.02	13.5, −6	1150	0.014	0.0	—
Unstable	15	6.8, 10	(304, 202, 154)	0.02	7.8, −1.8	1150	0.02	0.023	—
Stable	5	3.2, 8.6	(304, 202, 186)	0.008	5.0, −3.0	250	0.01	—	−0.5

TABLE 3 | Domain characteristics for the LES domain with the GAD for each stability case.

Case	Δx (m)	Δz_s, $\langle \Delta z \rangle$ (m)	(n_x, n_y, n_z) (—)	Δt (s)	z_0 (m)	$\overline{w'\theta'}_s$ (K m s^{-1})	$\dot{T}_s$ (K h^{-1})
Neutral	3	1.9, 9.4	(3008, 202, 154)	0.005	0.014	0.0	—
Unstable					0.02	0.023	—
Stable					0.01	—	−0.5

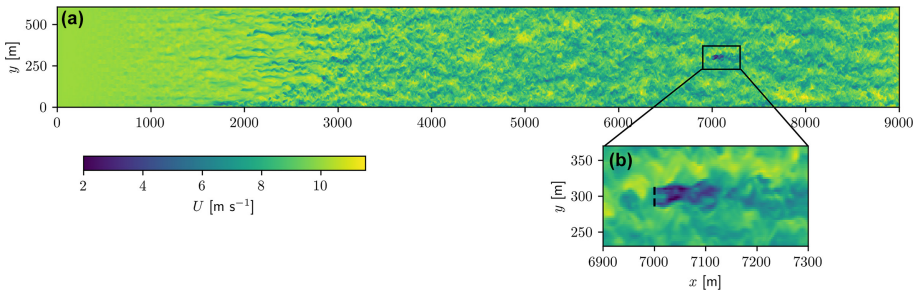

FIGURE 1 | Plan view of the instantaneous horizontal wind speed at hub height for the neutral stability case. Panel (b) zooms into the location of the GAD in the domain.

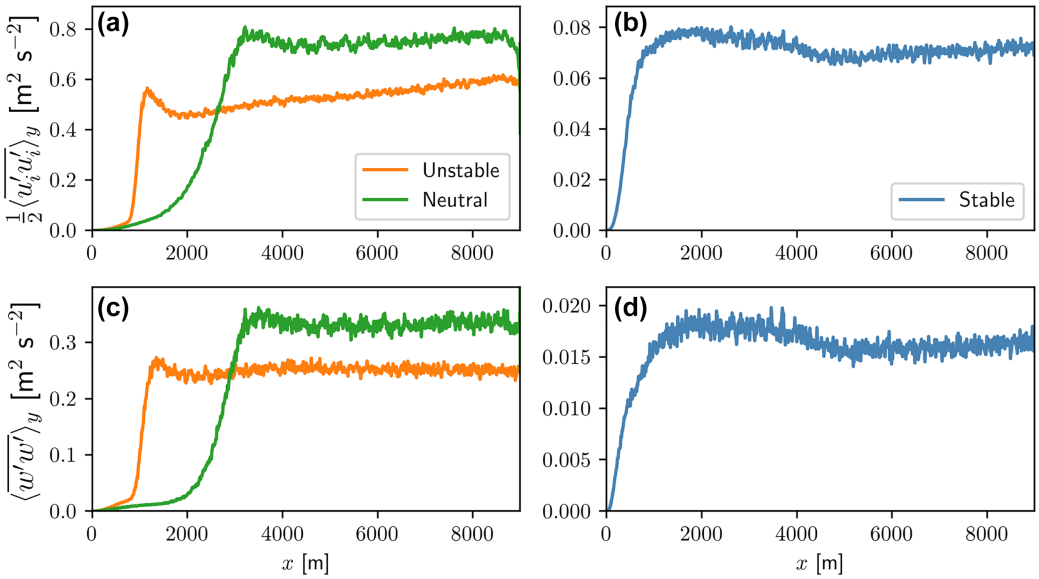

FIGURE 2 | Streamwise evolution of turbulence statistics at hub height ($z_h = 32$m) for each stability case in the high-resolution LES domain without the GAD. Note that turbulence statistics for the stable case (b, d) are shown in a different panel because they are one order of magnitude smaller than in the neutral and unstable simulations (a, c).

each stability condition, surface boundary conditions for the high-resolution run match those of the corresponding precursor run.

We use the cell-perturbation method [34, 35] to generate fully developed turbulence in the high-resolution LES domain. Stochastic potential temperature perturbations near the domain inflow boundary instigate vertical motions that efficiently transition into realistic turbulence structures downstream (Figure 1). Turbulence onset and equilibrium with the forcing is established within 1–4 km of fetch depending on the stability of the simulated boundary layer (Figure 2). We evaluate turbulence evolution across the domain using the TKE $\bar{k}$ and vertical velocity variance $\overline{w'w'}$ at hub height for the simulations without the GAD model. Turbulence at hub height develops faster for the unstable boundary layer (orange lines in Figure 2), consistent with findings from previous studies [36]. Even though hub-height TKE continually increases after 2 km of fetch in the unstable case, the vertical velocity variance stabilizes after 3 km. For the neutral case, turbulence statistics at hub height remain unchanged after 4 km. Interestingly, turbulence develops and stabilizes rapidly in the stable boundary layer, due to the high-resolution grid used that allows a rapid shear-triggered transition. We conservatively place the turbine at a location of

$x = 7000$ m from the inflow boundary, where turbulence has fully developed (Figure 1).

Mean inflow conditions to the GAD model in FastEddy are similar to other LES codes from Doubrawa et al. [18] and observations from the SWiFT campaign [20] (Figure 3). Mean wind speed for all stability conditions is well represented in the high-resolution LES. The root-mean-square deviation (RMSD) across the rotor layer between the observed and simulated wind speed is 0.27, 0.26, and 0.22 m s^{-1}, for the neutral, unstable, and stable conditions, respectively. Furthermore, the absolute percentage difference between the observed and simulated hub-height wind speed is 0.93%, 0.62%, and 6.2% for the neutral, unstable, and stable conditions, respectively. For reference, the mean absolute difference between the observed and simulated hub-height wind speed for the LES codes in Doubrawa et al. [18] is 0.99%, 1.9%, and 0.8% for the neutral, unstable, and stable conditions, respectively. The inflow wind direction to the turbine in the idealized FastEddy simulations is commensurate with the other LES codes. The wind direction changes minimally with height in the neutral and unstable cases within the lowest 60 m above the surface (< 2 from the reference hub-height wind direction), in agreement with the ensemble mean of observations. For the stable case,

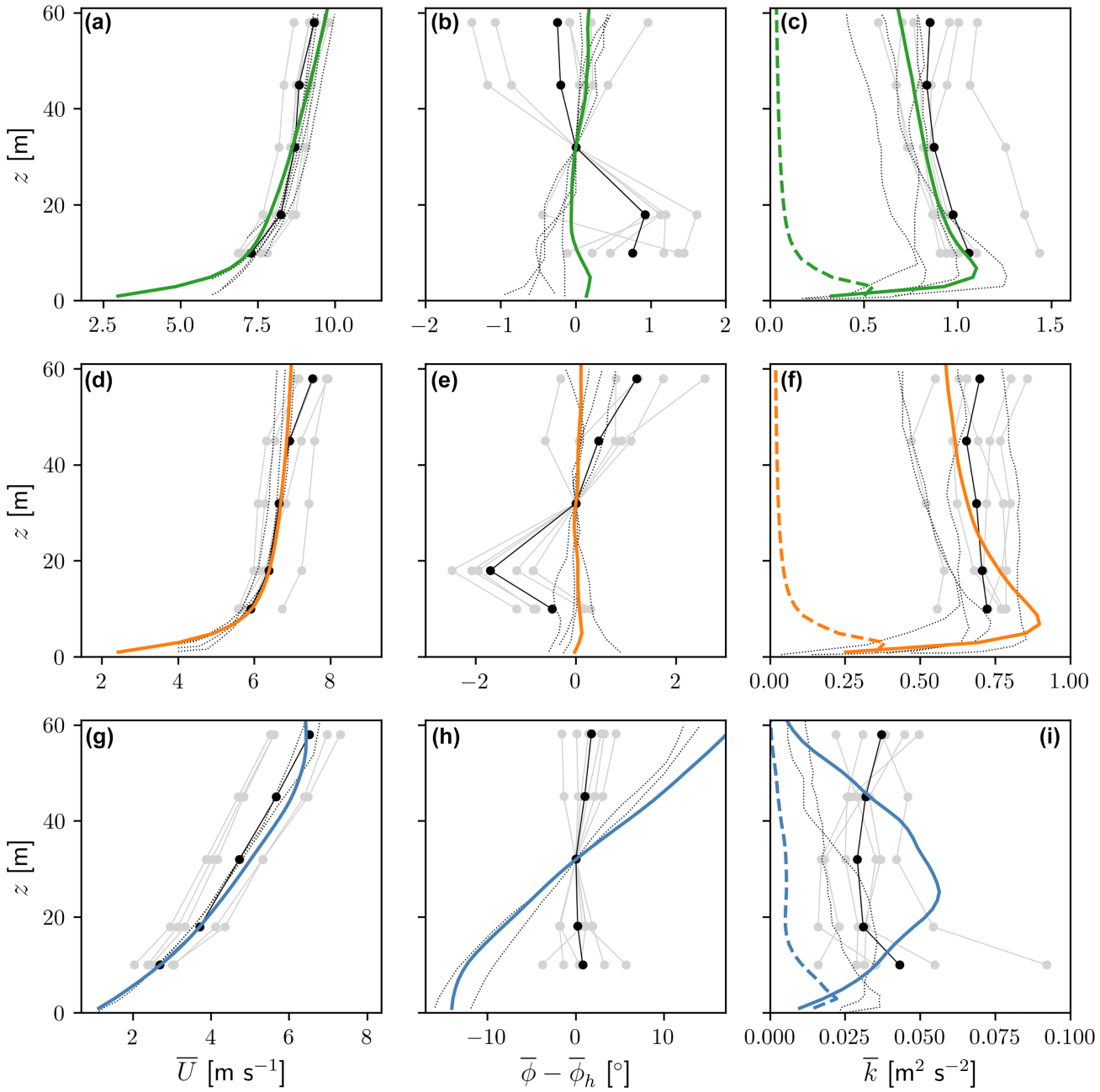

FIGURE 3 | Vertical profiles of the time-averaged horizontal wind speed $\overline{U}$ (a, d, g), wind direction relative to hub height $\overline{\phi} - \overline{\phi}_h$ (b, e, h), and resolved turbulence kinetic energy $\overline{k}$ (c, f, i) at $x = 7000$ m (i.e., the location of the turbine) in the simulations without the GAD. Results are shown for the neutral (a–c), unstable (d–f), and stable (g–i) simulations. Ten-minute averaged observations are shown in light gray and the ensemble mean in black. Simulation results for the LES codes in [18] are shown for reference using dotted lines. Modeled turbulence kinetic energy in panels (c, f, i) is shown as the dashed colored lines for each stability case for completeness.

wind direction changes with height (i.e., wind veer) across the turbine rotor layer, like in the LES codes in Doubrawa et al. [18] and Kale et al. [21]. Remarkably, the inflow wind profiles for the stable conditions at the SWIFT site display minimal wind veer.

Turbulence in the turbine rotor layer is also well represented in the FastEddy simulations (Figure 3c,f,i). The RMSD between the observed and simulated (resolved) TKE across the turbine rotor layer is 0.084, 0.089, and 0.018 $m^2\ s^{-2}$, for the neutral, unstable, and stable conditions, respectively. The absolute percentage difference between hub-height TKE in the observations and simulations amounts to 5.7%, 4.3%, and 77.3% for the neutral, unstable, and stable conditions, respectively. While turbulence variability is larger in our stable simulation relative to the ensemble mean of observations, it is still within the variability of observed TKE. Doubrawa et al. [18] and Kale et al. [21] also report larger errors in replicating the observed turbulence characteristics for the stable conditions compared to the neutral and unstable cases. To illustrate, hub-height TKE in the stable simulations from SOWFA is 40% smaller than the ensemble mean of observations, but only 12% for the neutral and unstable conditions [18]. Furthermore, at least 90% of the total (resolved plus modeled) TKE above $z = 18$ m is resolved for the three stability cases, indicative of proper and well resolved atmospheric LES simulations (e.g., [37]). Differences in the mean flow and turbulence statistics between the observations and simulations highlight the challenges of reproducing real-world conditions using idealized simulations, especially for stable boundary layers.

4 | Validation of the GAD in FastEddy

We validate the GAD implementation in FastEddy using wake velocity observations and wind-turbine performance metrics. The wake evolution downstream of the turbine is compared against lidar observations and other LES codes for the three stability cases. Furthermore, the power production measured from the generator in the wind turbine is compared against the simulated results.

4.1 | Wake Development

The GAD model in FastEddy produces a rotating wake downstream of the turbine (Figure 4). The cross-section at $x/D = 1.3$

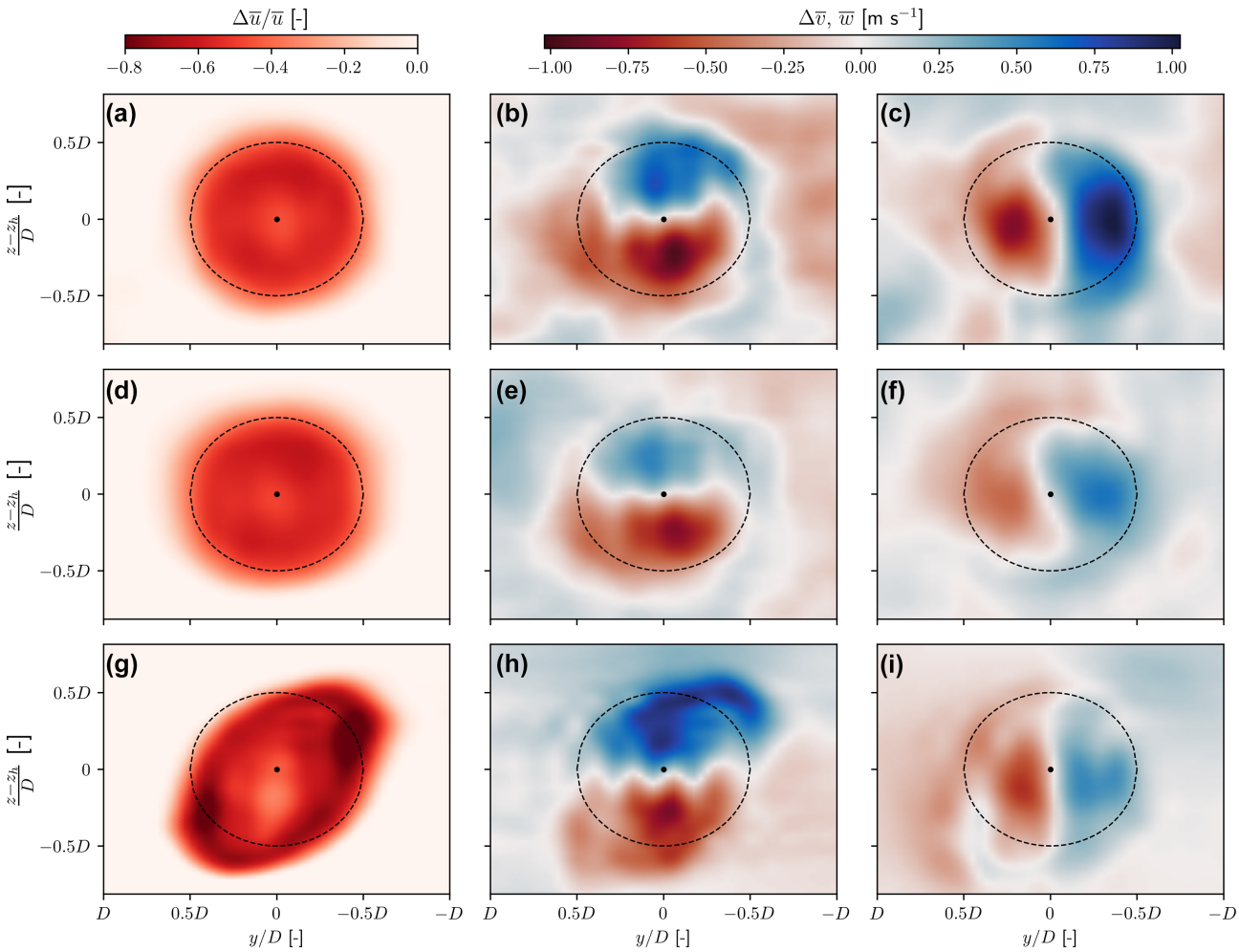

FIGURE 4 | Time-averaged cross sections of the normalized u-velocity deficit $\Delta\overline{u}/\overline{u}$ (a, d, g), the v-velocity deficit $\Delta\overline{v}$ (b, e, h), and the vertical velocity $\overline{w}$ field (c, f, i). Model results for the neutral simulation are shown in panels (a–c), unstable simulation in panels (d–f), and stable simulation in panels (g–i). Mean wind conditions are plotted at $x/D = 1.3$ downstream of the turbine location. The dashed black line mark the turbine-rotor perimeter, and the central black dot represents the hub height. Note that the wake is seen from an upstream perspective.

in Figure 4 of velocity differences relative to the reference velocity from the LES without the turbine illustrates the vertical and cross-stream velocities induced by the turbine. As expected, wake rotation downstream of the GAD is opposite to the turbine-rotation direction. Modern wind turbines rotate clockwise from an upstream perspective, as a result, their wakes rotate in a counter-clockwise direction.

The shape of the turbine wake depends on atmospheric stability. In stable conditions, veering of the wind with height across the turbine rotor diameter deforms the wake along the cross-stream direction, while wake rotation advects the wake vertically, leading to an elliptical pattern (Figure 4g), as previously observed in field measurements [38, 39] and simulations [40–42]. Wind veer is minimal in the neutral and unstable cases; consequently, the velocity deficit in the wake follows a circular pattern (Figure 4a,d), as also shown in Kale et al. [21].

Turbulence generation and transport in the wake of the turbine also varies with atmospheric stability (Figure 5). We examine the dominant terms in the TKE budget to provide insight into the physical processes that modify wake expansion and recovery. To this end, we consider the balance between TKE advection by the mean flow (i.e., $-\overline{u}_i \partial \overline{k}/\partial x_i$), TKE production from shear (i.e., $-\overline{u_i' u_j'}\, \partial \overline{u}_i/\partial x_j$), turbulent transport of TKE (i.e., $-\partial \overline{u_i' k}/\partial x_j$), and turbulence dissipation (i.e., $-\varepsilon$). We do not include TKE generation/suppression from buoyancy because it is two orders of magnitude smaller than the other terms in the wake region. Turbulence generation immediately downstream of the turbine is primarily caused by shear as tip vortices promote mixing at the interface between the wake and the surrounding flow (Figure 5b,f,j). For the neutral and unstable cases, shear production is largest immediately downstream of the turbine ($x/D < 2$) and is for the most part balanced by mean flow and turbulent transport of TKE. Increased turbulent conditions in the neutral and unstable cases enable turbulent entrainment of TKE from the ambient flow immediately downstream of the turbine. For the stable simulation, mean flow advection and viscous dissipation balance shear generation for $x/D < 2$, while turbulence transport plays a minor role because turbulence from the ambient flow is small. Farther downstream of the turbine in the neutral and unstable conditions ($x/D > 2.5$), shear generation plays a lesser role as mean flow advection is balanced by turbulent entrainment of TKE. Conversely, shear generation remains significant between $x/D = 2$ and $x/D = 5$ in the stable case and is balanced by mean flow and turbulent transport of TKE. Note that the unstable simulation features a weak surface heat flux of ≈ 20 W m^{-2}, and therefore, turbulent mixing is only moderately different from that of the neutral boundary layer simulation.

The instantaneous velocity field illustrates different mechanisms that regulate wake recovery downstream of the turbine in each case (Figure 6). Wake meandering in the unstable and neutral simulations starts immediately downstream of the turbine, evolving into vortex shedding farther downstream (Figure 6a,c). Coherent roll structures also increase mixing in the unstable simulation. The convective roll structures that develop in the surface layer of the unstable simulation mix the wake more efficiently with the surrounding flow in the unstable case than in the neutral case (Figure 6c,d). Low ambient turbulence in the stable simulation inhibits mixing and wake meandering immediately downstream of the turbine; however, small vortices form at the interface between the wake and the surrounding flow that promote mixing (Figure 6e,f). These results provide an initial qualitative validation of the flow response to the presence of the turbine.

A quantitative evaluation of the wake structure measured as velocity deficit is provided by comparing to the lidar observations

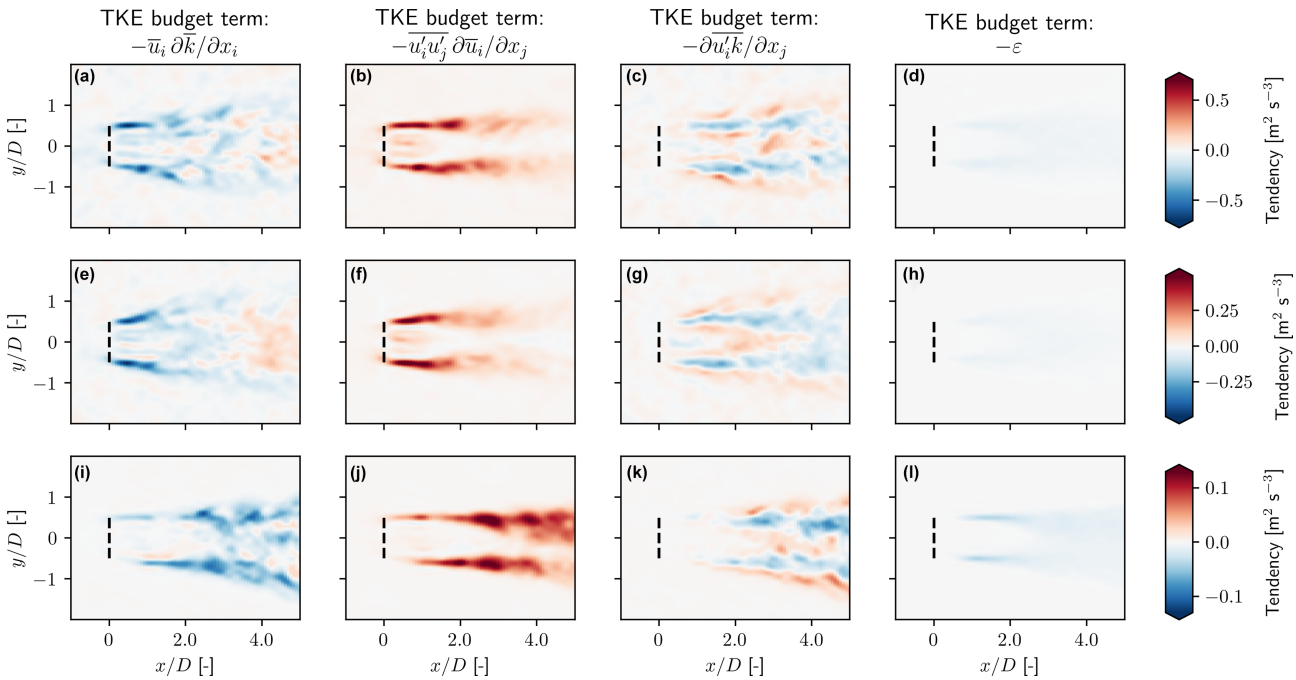

FIGURE 5 | Hub-height TKE budget for the neutral (a–d), unstable (e–h), and stable (i–l) atmospheric conditions. Panels (a, e, i) correspond to TKE advection by the mean flow, panels (b, f, j) to TKE shear production, panels (c, g, k) to turbulent transport of TKE, and panels (d, h, l) to viscous dissipation of TKE. The dashed black line marks the location of the turbine in the domain.

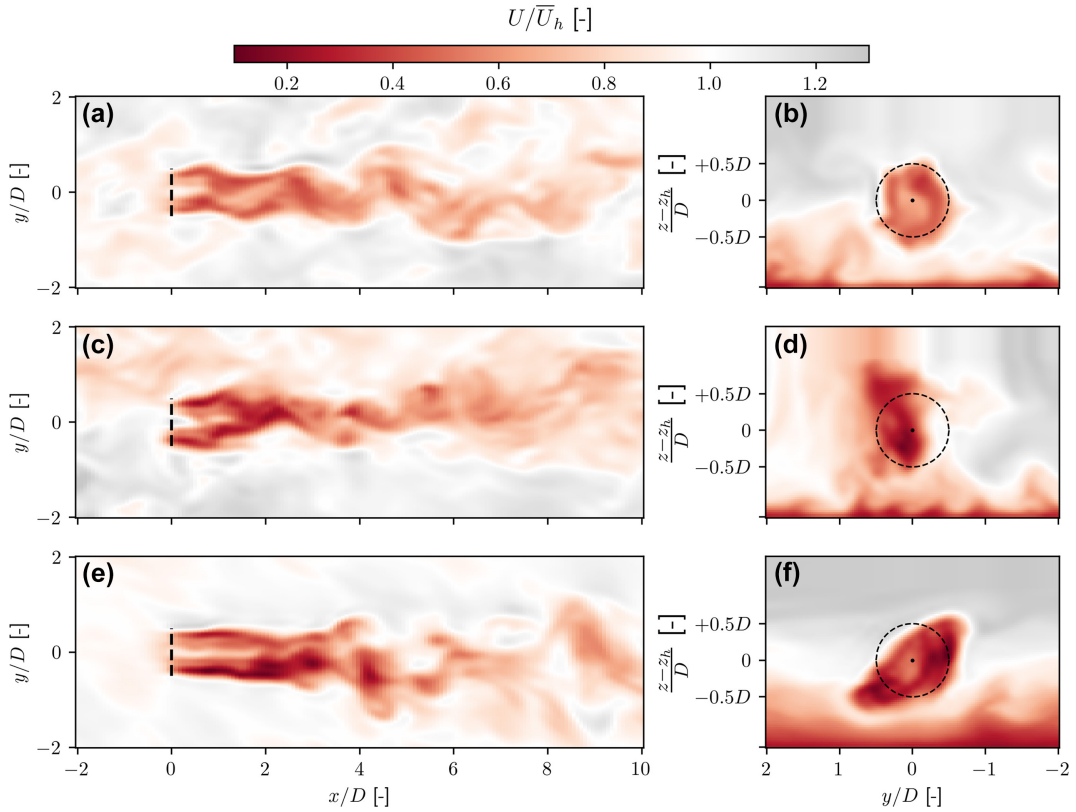

FIGURE 6 | Instantaneous normalized horizontal wind speed for the neutral (a, b), unstable (c, d), and stable simulations (e, f). The vertical slices in panels (b, d, f) correspond to $x/D = 2$. The location of the turbine in the domain is represented by the dashed black line. The instantaneous wind speed is normalized by the time-averaged hub-height velocity at the turbine location in the simulation without the GAD for the corresponding stability case.

and the other LES codes in Doubrawa et al. [18]. We define the horizontal wind speed deficit $\Delta\overline{U} = \overline{U}_{\text{GAD}} - \overline{U}_{\text{noGAD}}$ as the difference in the time-averaged velocity field between the simulation with ($\overline{U}_{\text{GAD}}$) and without ($\overline{U}_{\text{noGAD}}$) the turbine in the domain.

The velocity deficit in the wake of the FastEddy GAD agrees with other LES codes and with observations, capturing the distinct evolution of the wake for each stability case (Figure 7). The turbine wake persists farther downstream in the neutral and stable conditions compared to the unstable conditions. Convective rolls enhance mixing in the unstable case, resulting in a 20% maximum hub-height velocity deficit $5D$ downstream of the GAD. Conversely, the maximum velocity deficit at hub height is 30% and 35% for the neutral and stable cases, respectively, due to reduced mixing. Asymmetries in the hub-height velocity deficit in the far wake of the GAD for the stable conditions are attributed to wind veer. Wind veer is larger in our simulations than in the observations (Figure 3h), contributing to deforming the wake in an elliptical pattern and to producing an asymmetric velocity deficit at hub height. As expected, model results and observations show the velocity deficit at hub height is strongest close to the turbine ($x/D = 2$) and weakest downstream ($x/D = 5$). The width of the wake is also similar in FastEddy compared to the other LES and the scanning lidar observations. As expected, the wake is narrower close to the turbine and expands (i.e., recovers) downstream due to mixing through ambient turbulence. Differences in wake expansion in the far wake of the turbine for the stable case between our simulations and the observations are likely due to increased lateral entrainment of TKE due to enhanced ambient turbulence.

We evaluate the skill of the FastEddy GAD in capturing the effects of the wind turbine on the flow using the total velocity deficit in the wake. Here, the total velocity deficit in the wake of the turbine at hub height $VD(x^*)$ is defined using Equation (1), where $y^* = y/D$ and $\Delta\overline{U}$ is the horizontal wind speed deficit at $x^* = x/D$ downstream of the turbine. Note that we report the relative difference between the total velocity deficit from observations and simulations, normalized by the observed velocity deficit.

$$VD(x^*) = \int_{-1}^{1} \Delta\overline{U}(x^*)\,dy^* \tag{1}$$

The implementation of the GAD model in FastEddy provides an accurate representation of the effect of the wind turbine in the flow for neutral, unstable, and stable conditions (Figure 8). The total velocity deficit in the near wake of the turbine ($x/D \leq 3$) in FastEddy displays minimal differences with respect to observations for all stability conditions. Farther downstream, where atmospheric conditions regulate wake development, wake evolution in FastEddy is comparable to other LES codes. In general, the LES models represent the near wake of the turbine more effectively than the far wake, possibly due to disparities in simulated atmospheric conditions across LES

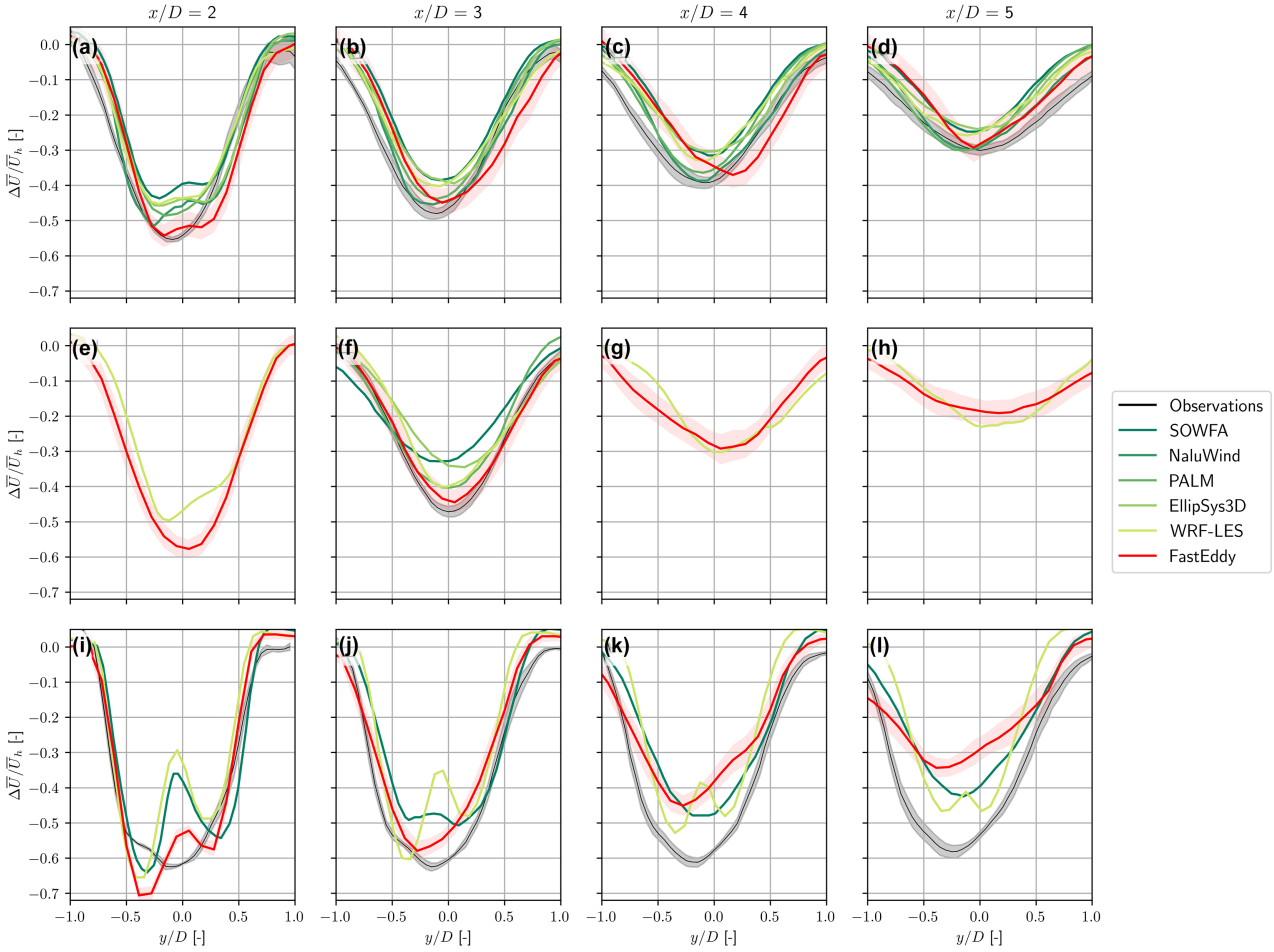

FIGURE 7 | Streamwise evolution of the normalized horizontal wind speed deficit at hub height for each model and observations in the neutral (a–d), unstable (e–h), and stable (i–l) benchmarks. Panels (a, e, i) correspond to $x/D = 2$, panels (b, f, j) to $x/D = 3$, panels (c, g, k) to $x/D = 4$, and panels (d, h, l) to $x/D = 5$. The shaded regions represent the 95% confidence interval for the FastEddy simulations and the observations. Note that not all models provide results for the three stability cases.

models. For the neutral simulation in FastEddy, the maximum velocity deficit in the far wake ($x/D = 5$) is in good agreement with the maximum velocity deficit from the observations (Figure 7d). However, higher momentum entrainment from the ambient flow reduces the wake's width in the simulations as compared to the observations. The largest differences in the velocity deficit between FastEddy and observations occur during stable conditions (Figure 8h,i). The velocity deficit at $x/D = 4$ and $x/D = 5$ in the stable simulation shows a wider wake compared to the observations and the other LES codes (Figure 7k,l). It is likely that the increased turbulence at hub height in the FastEddy simulations increases the lateral entrainment due to turbulence mixing compared to the observations. Moreover, increased wind veer in the simulations also produces larger asymmetries in the wake as compared to the observations.

4.2 | Wind Turbine Performance

We compare the wind turbine response to atmospheric conditions from the FastEddy GAD against observations and other LES codes. Turbine rotational speed, generator power, and generator torque from field measurements serve as ground truth for assessment of model results. The GAD in FastEddy does not employ a wind turbine controller, therefore we estimate generator power by multiplying the aerodynamic power by the electrical efficiency of the generator in the Vestas V27 wind turbine ($\eta = 0.944$), as in Kale et al. [21]. To estimate generator torque, we employ the generator efficiency as well as the gearbox ratio from the turbine rotor to the generator (27.565) following the approach of Kale et al. [21]. Finally, we also compare the turbine's thrust coefficient from FastEddy with other LES codes. For the observations, we estimate the aerodynamic thrust coefficient using the inflow hub-height wind speed recorded from the met-tower and the turbine's theoretical thrust curve [43].

Turbine performance in the FastEddy GAD is within the variability of observations and similar to other LES codes (Figure 9). Turbine-performance metrics (i.e., turbine rotational speed, generator power, and generator torque) from FastEddy are generally within one standard deviation of the observations. Moreover, the 95% confidence interval in generator power from the FastEddy GAD encompasses the mean generator power from the observations for the neutral

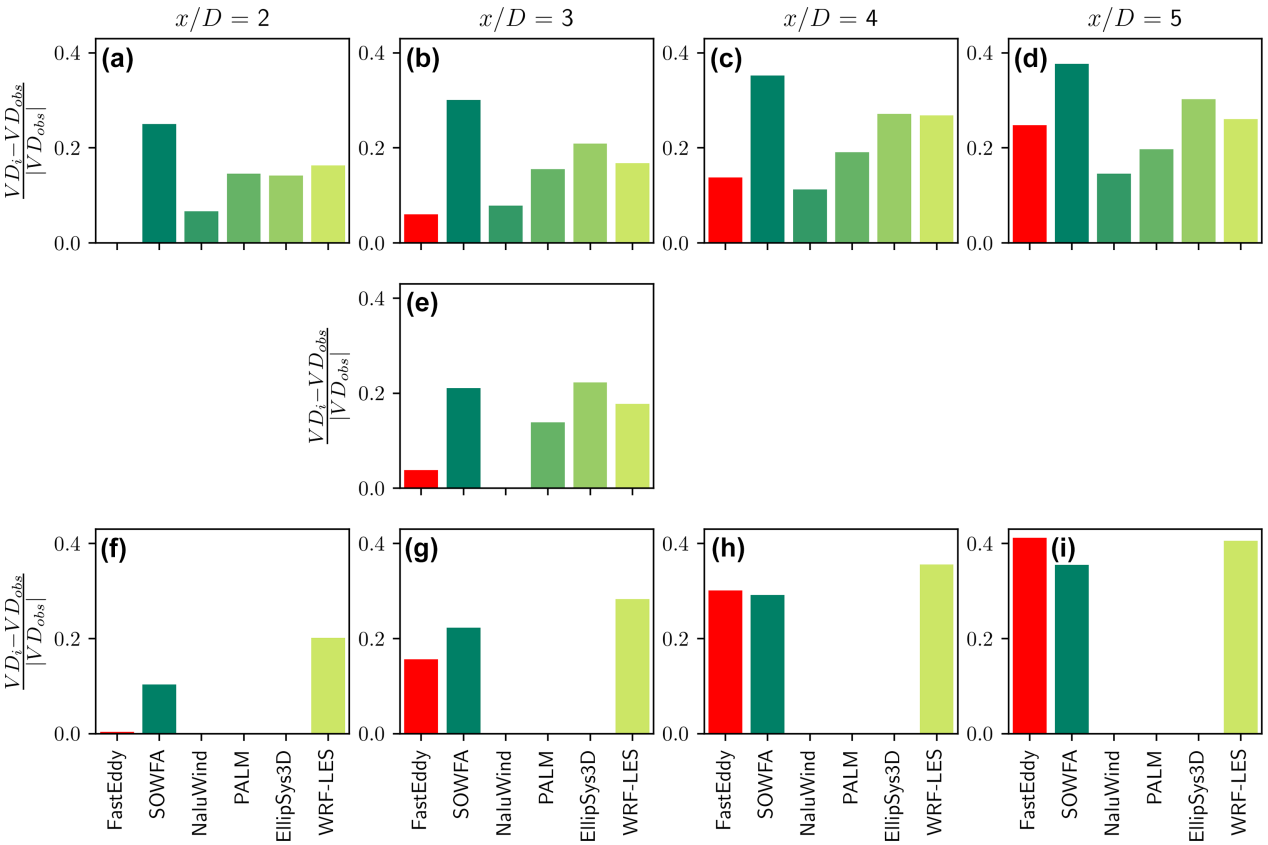

FIGURE 8 | Total velocity deficit in the wake for each model, normalized by the observed velocity deficit, in the neutral (a–d), unstable (e), and stable (f–i) benchmarks. Panels (a, f) correspond to $x/D = 2$, panels (b, e, g) to $x/D = 3$, panels (c, h) to $x/D = 4$, and panels (d, i) to $x/D = 5$. Note that results for the unstable case are only shown at one distance downstream because wake measurements are only available at $x/D = 3$.

and unstable simulations. Like other LES codes, the GAD in FastEddy overestimates generator power for stable conditions by 32%, partly because the turbine's rotational speed is faster than in the SWiFT turbine. The current implementation of the GAD in FastEddy uses freestream wind speed as an input to the GAD parameterization; thus, the turbine rotational speed remains constant throughout the simulations (note the lack of error bar in the left-most panels for FastEddy results).

4.3 | Computational Cost

Following the approach from Doubrawa et al. [18], we quantify the relative performance of FastEddy compared to other LES codes and other more simplified models that participated in the benchmark exercise. Following Doubrawa et al. [18], we use as a summary model accuracy metric the root-sum-square of the differences between the simulated and measured velocity deficit profiles, normalized by the root-sum-square of the measured velocity deficit (Equation 2). In Equation (2), ξ represents the lateral $y^* = y/D$ or vertical $z^* = z/D$ direction to capture the differences in the lateral and vertical wake profiles. The root-sum-square is calculated at each $x^* = x/D$ location downstream between $x/D = 2$ and $x/D = 5$ in $1D$ increments, then aggregated for all downstream distances. The average of the vertical ($\mathbb{E}_{z^*}$) and lateral ($\mathbb{E}_{y^*}$) differences in the wake profile are reported in Figure 10. Using a single skill metric value for the entire wake may be too simplistic to accurately depict the nature of the differences between the different LES codes. Some models, like FastEddy and Naluwind, may skillfully predict the wake close to the turbine (Figure 8a) but yield larger differences with the observations farther downstream (Figure 8c). Conversely, other models, such as PALM, show similar skill at predicting the velocity deficit in the near and far wake of the turbine. Difficulty in representing the velocity deficit in the far wake is likely due to the specific atmospheric forcing used by each LES given that ambient conditions have non-negligible impact on wake development.

As a reference to estimate the computational cost of each simulation, we use the wall-clock time required to complete 10 min of simulation multiplied by the number of processing units, like in Doubrawa et al. [18]. Following the approach from previous studies that compare the performance of CPU- and GPU-based LES codes [44–46], we consider the number of processing units as the number of CPU-cores and GPUs employed for each simulation. We only show the error versus computational cost for the neutral stability simulation since Doubrawa et al. [18] did not report cost estimates from the other stability cases.

$$\mathbb{E}_{\xi} = \sum_{x^*} \frac{\sqrt{\sum_{\xi} \left[\Delta\overline{U}_i - \Delta\overline{U}_{obs}\right]^2}}{\sqrt{\sum_{\xi} \Delta\overline{U}_{obs}^2}} \tag{2}$$

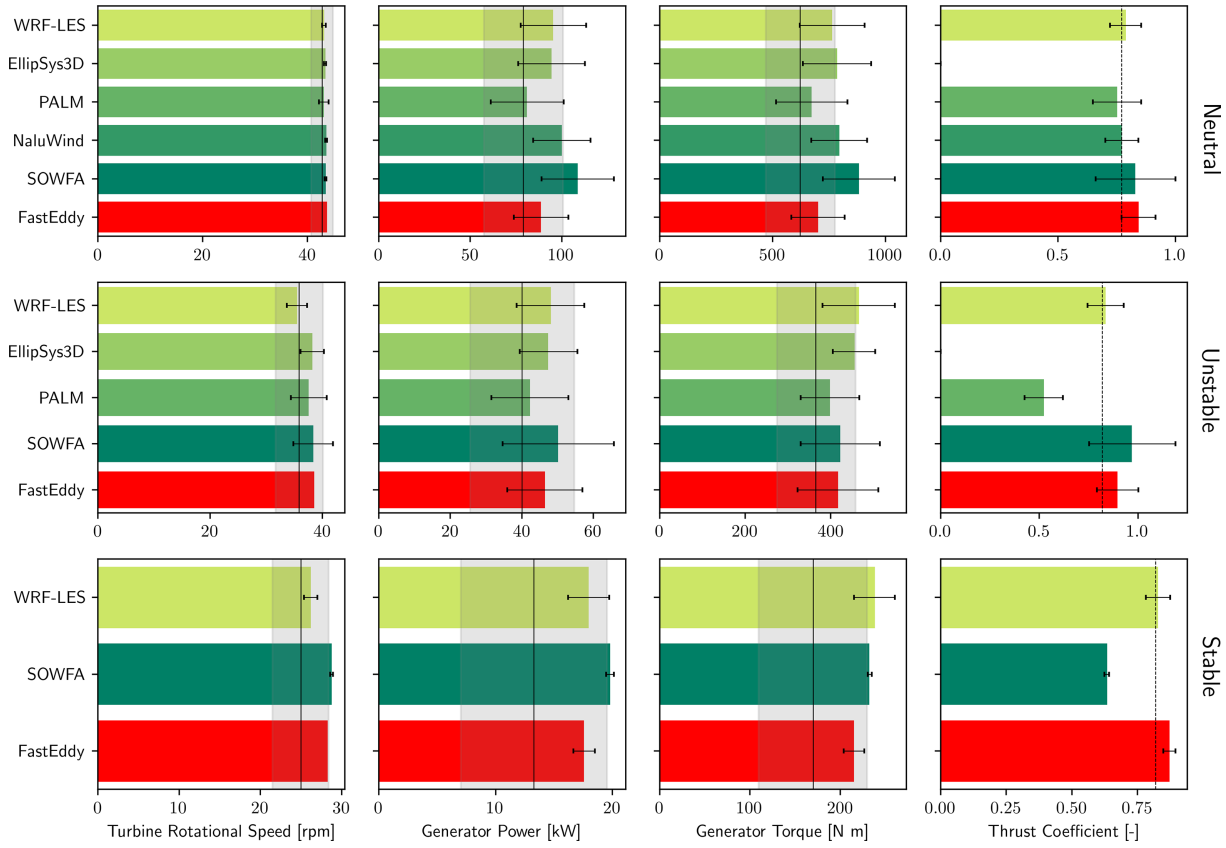

FIGURE 9 | Mean and standard deviation for time series of turbine-performance metrics for the neutral (top panels), unstable (middle panels), and stable (bottom panels) benchmarks. Simulation results are shown by colored bars (mean value) and horizontal black line (standard deviation). Measured values are shown by vertical black lines (mean) and gray shading (standard deviation). Note that the thrust coefficient is not measured in the field, but rather estimated from the OpenFAST model.

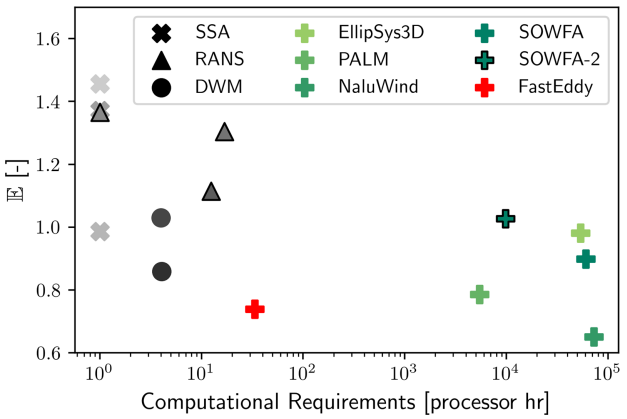

FIGURE 10 | Cumulative error for each simulation approach as a function of computational cost for the neutral benchmark. Shown in color are results for the LES as presented in Doubrawa et al. [18]. In shades of gray are model performance for steady-state analytical (SSA), dynamic wake meandering (DWM), and Reynolds-averaged Navier stokes (RANS) simulations as presented in Doubrawa et al. [18]. The computational cost is given in processor hours for a 10-min long wake simulation that does not include spinup time. Note that the computational cost is highly dependent on grid resolution, time step, and number of grid points, which differ in all models. Also, two data points are shown for SOWFA as different model configurations are reported in Doubrawa et al. [18].

FastEddy achieves accuracy comparable to the other LES with significantly lower computational cost (Figure 10). For completeness, Figure 10 presents results for LES (colored symbols), steady-state analytical (SSA) models (light gray x markers), Reynolds-Averaged Navier Stokes (RANS) models (gray triangles), and dynamic wake meandering (DWM) models (dark gray circles), as reported in Doubrawa et al. [18]. We do not show the computational cost from the WRF-LES model since it was not reported in Kale et al. (2022) [21]. The neutral boundary layer simulation in FastEddy required 2 h 49 min of wall time to complete 10 min of simulation on 12 NVIDIA Tesla V100 GPUs, while writing full-domain three-dimensional output every 10^4 time steps. It is worth reiterating that the computational cost shown in Doubrawa et al. [18] and reported here represents the performance from each model as it was configured and run. Of importance, the other LES codes in Figure 10 may employ a finer, minimum grid spacing than FastEddy to properly model the SWiFT turbine using an Actuator Line parameterization. Additionally, the total degrees of freedom (or number of grid cells) varied across LES configuration by several orders of magnitude. Consequently, Figure 10 does not facilitate a direct comparison of optimal code performance, rather only a relative modeling cost for each model configured to achieve the common primary objective of validation against the SWiFT benchmark cases (rather than

optimal computational performance or prediction rate). That said, the computational requirement for FastEddy is two to three orders of magnitude smaller than any of the other CPU-based LES codes and rather comparable to computational cost of RANS models while achieving significantly lower error (almost a factor of two). This is consistent with the GPU to CPU performance gain of 256 CPU-cores reported by Sauer and Muñoz-Esparza [10]. Moreover, at this ratio of GPUs to CPU-cores (and using optimal scaling of the CPU code), FastEddy still achieves 6 times faster prediction rate under equivalent power, or 8 times lower power consumption at an equivalent CPU/GPU prediction rate. Performance benefits from FastEddy stem from carrying out all time-dependent calculations, including those from the GAD, on GPU [10], avoiding large data transfers between the CPU and GPU memory spaces for advancing the simulation. In this manner, the GAD model results in minor performance reductions to the FastEddy code. For the domain configuration employed here, the GAD model increased wall time per time step on average by 0.88% as compared to the simulation without a turbine in the domain (average over 10^5 time steps). Nevertheless, the computational cost of running the GAD in FastEddy will depend on the domain size and number of turbines in the simulation. We acknowledge that optimal configuration of CPU-based LES models could perhaps improve the 'computational requirements' by some factor, however we would not expect such optimizations to achieve even one order of magnitude in the best case. It is anticipated that such performance will be even more appealing for the LES models when considering turbulence quantities, since eddies are explicitly resolved instead of fully parameterized. This comparison demonstrates how efficient, GPU-resident LES models establish a viable new standard in the wind energy community for computationally practical and undeniably superior accuracy.

5 | Summary and Conclusions

We have successfully validated an implementation of the GAD model in FastEddy against observational data and other LES codes. We benchmark the GAD in FastEddy against data from the SWiFT facility in Lubbock, Texas for a variety of atmospheric conditions. Wind speed measurements from a meteorological tower located upstream of a scaled wind turbine, a downstream-pointing nacelle-mounted lidar and turbine-performance measurements recorded at the SWiFT facility were used to validate the GAD in FastEddy for neutral, weakly unstable and stable atmospheric conditions. The GAD model in FastEddy is capable of simulating and predicting the aerodynamic behavior of a wind turbine within its operational environment commensurate with other LES codes and in good agreement with the observations.

The GAD model in FastEddy accurately represents the effect of a wind turbine on the surrounding flow. The turbine parameterization in FastEddy produces a counter-clockwise rotating wake, as seen from an upstream perspective, that persists farther downstream in stable conditions compared to neutral and weakly unstable conditions. Moreover, the velocity deficit in the wake of the turbine in FastEddy is comparable to observations and commensurate in accuracy to other LES codes and turbine parameterizations, including Actuator Line models. The velocity deficit in the near wake of the turbine ($x/D \leq 3$), where the effect from the turbine is most pronounced, is well represented in FastEddy compared to lidar measurements for neutral, weakly unstable, and stable conditions. Farther downstream, where turbulence mixing becomes increasingly more dominant for wake development, the velocity deficit in FastEddy is comparable to other LES codes and turbine models. Differences in the velocity deficit in the far wake between FastEddy and the observations are likely caused by discrepancies in atmospheric forcing between models.

Not only is the effect of the turbine on the flow accurate, the wind turbine response to atmospheric conditions is also well represented in the FastEddy GAD. The turbine's rotational speed, power, and torque in the GAD model in FastEddy are similar to the observations and commensurate with other LES codes for neutral, unstable and stable conditions. The turbine thrust, the main driver of the velocity deficit in the wake, is also well matched in the FastEddy GAD versus the theoretical thrust of the scaled turbine and the other LES model results.

This new GAD model implementation in FastEddy enables fast and accurate turbulence-resolving simulations of wind turbines in realistic atmospheric flows. FastEddy's GAD yields accuracy comparable to other LES codes, yet at a dramatically lower computational cost. The implementation of the GAD and scalability of FastEddy also provides a viable path forward to tackle large-scale problems, such as investigating farm-to-farm interactions, or studying the interaction of wind turbines with the atmospheric boundary layer on longer time scales (i.e., days) including ensemble LES simulations. Performant turbulence-resolving wind turbine simulations may also enable real-time wind farm control. Real-time LES-informed controllers may enable power gains in large wind farms by leveraging dynamic yaw steering inside the turbine cluster [47]. Ongoing work to incorporate a yaw controller into the GAD routine will allow performing LES of wind turbines under coupled mesoscale-microscale or multi-scale time/space-varying atmospheric real-world conditions for which FastEddy has already shown ample skill and performance capacity [12–14].

Acknowledgments

The authors want to express their greatest gratitude to Dr. Branko Kosović and Prof. Julie K. Lundquist for technical insights and facilitating this collaborative research effort. The authors would also like to thank Dr. Paula Doubrawa for providing the experimental data for the three SWiFT benchmarks and the modeling data for the code-to-code comparison. This work was authored in part by the National Renewable Energy Laboratory, operated by Alliance for Sustainable Energy, LLC, for the US Department of Energy (DOE) under Contract No. DE-AC36-08GO28308. Funding is provided by the US Department of Energy Office of Energy Efficiency and Renewable Energy Wind Energy Technologies Office. The views expressed in the article do not necessarily represent the views of the DOE or the US Government. The US Government retains and the publisher, by accepting the article for publication, acknowledges that the US Government retains a nonexclusive, paid-up, irrevocable, worldwide license to publish or reproduce the published form of this work, or allow others to do so, for US Government purposes. Contributions from DME and JAS were funded by the 2022 NCAR Research Applications Laboratory (RAL)

Opportunity Award: "Wind Energy Solutions with FastEddy®." The authors would like to acknowledge high-performance computing support from Casper/Cheyenne (doi:10.5065/D6RX99HX) and Derecho (doi:10.5065/qx9a-pg09) provided by NCAR's Computational and Information Systems Laboratory (CISL), sponsored by the National Science Foundation.

Data Availability Statement

The instantaneous hub-height velocity fields for each stability case presented here are available at Sanchez Gomez, Sauer, and Muñoz Esparza [48]. An open source version of the FastEddy dynamical core is available via a public github: https://github.com/NCAR/FastEddy-model. The GAD extension to FastEddy used in this manuscript is planned to be included in the public version in a future release cycle. In the meantime, collaborative access to the GAD-inclusive FastEddy model may be granted upon request for research through the Research Applications Laboratory at the National Center for Atmospheric Research (https://ral.ucar.edu/solutions/products/fasteddy).

Peer Review

The peer review history for this article is available at https://www.webofscience.com/api/gateway/wos/peer-review/10.1002/we.2941.

References

1. R. Stoll, J. A. Gibbs, S. T. Salesky, W. Anderson, and M. Calaf, "Large-Eddy Simulation of the Atmospheric Boundary Layer," *Boundary-Layer Meteorology* 177, no. 2–3 (2020): 541–581.

2. Y. T. Wu and F. Porté-Agel, "Atmospheric Turbulence Effects on Wind-Turbine Wakes: An LES Study," *Energies* 5, no. 12 (2012): 5340–5362.

3. M. J. Churchfield, S. Lee, J. Michalakes, and P. J. Moriarty, "A Numerical Study of the Effects of Atmospheric and Wake Turbulence on Wind Turbine Dynamics," *Journal of Turbulence* 13 (2012): N14.

4. W. Chanprasert, R. N. Sharma, J. E. Cater, and S. E. Norris, "Large Eddy Simulation of Wind Turbine Fatigue Loading and Yaw Dynamics Induced by Wake Turbulence," *Renewable Energy* 190 (2022): 208–222.

5. K. Wu and F. Porté-Agel, "Flow Adjustment Inside and Around Large Finite-Size Wind Farms," *Energies* 10, no. 12 (2017): 2164, http://www.mdpi.com/1996-1073/10/12/2164.

6. M. Sanchez Gomez, J. K. Lundquist, J. D. Mirocha, and R. S. Arthur, "Investigating the Physical Mechanisms That Modify Wind Plant Blockage in Stable Boundary Layers," *Wind Energy Science* 8, no. 7 (2023): 1049–1069.

7. O. Maas, "From Gigawatt to Multi-Gigawatt Wind Farms: Wake Effects, Energy Budgets and Inertial Gravity Waves Investigated by Large-Eddy Simulations," *Wind Energy Science* 8, no. 4 (2023): 535–556, https://wes.copernicus.org/articles/8/535/2023/.

8. J. Schalkwijk, E. J. Griffith, F. H. Post, and H. J. J. Jonker, "High-Performance Simulations of Turbulent Clouds on a Desktop PC: Exploiting the GPU," *Bulletin of the American Meteorological Society* 93, no. 3 (2012): 307–314.

9. C. C. Van Heerwaarden, B. J. H. Van Stratum, T. Heus, J. A. Gibbs, E. Fedorovich, and J. P. Mellado, "Microhh 1.0: A Computational Fluid Dynamics Code for Direct Numerical Simulation and Large-Eddy Simulation of Atmospheric Boundary Layer Flows," *Geoscientific Model Development* 10, no. 8 (2017): 3145–3165.

10. J. A. Sauer and D. Muñoz-Esparza, "The FastEddy® Resident-GPU Accelerated Large–Eddy Simulation Framework: Model Formulation, Dynamical–Core Validation and Performance Benchmarks," *Journal of Advances in Modeling Earth Systems* 12, no. 11 (2020): e2020MS002100.

11. D. Muñoz-Esparza, J. A. Sauer, A. A. Jensen, L. Xue, and W. W. Grabowski, "The FastEddy ® Resident–GPU Accelerated Large–Eddy Simulation Framework: Moist Dynamics Extension, Validation and Sensitivities of Modeling Non–Precipitating Shallow Cumulus Clouds," *Journal of Advances in Modeling Earth Systems* 14, no. 4 (2022): e2021MS002904.

12. D. Muñoz-Esparza, H. H. Shin, J. A. Sauer, et al., "Efficient Graphics Processing Unit Modeling of Street-Scale Weather Effects in Support of Aerial Operations in the Urban Environment," *AGU Advances* 2, no. 2 (2021): e2021AV000432.

13. B. Kosovic, J. Sauer, D. Munoz-Esparza, and P. Hawbecker, "Coupled Mesoscale to Microscale Simulations of a Flow Over Complex Terrain Using the GPU Based LES Model FastEddyÒ Coupled With the Weather Research and Forecasting Model," in *AGU Fall Meeting Abstracts*, Vol. 2022, (2022), A43C–04.

14. D. Muñoz-Esparza, J. A. Sauer, P. Jiménez, J. Boehnert, D. Hahn, and M. Steiner, "Multiscale Weather Forecasting Sensitivities to Urban Characteristics and Atmospheric Conditions During a Cold Front Passage Over the Dallas-Fort Worth Metroplex," *Urban Climate (in review)* (2024), https://doi.org/10.2139/ssrn.4756851.

15. Y. T. Wu and F. Porté-Agel, "Large-Eddy Simulation of Wind-Turbine Wakes: Evaluation of Turbine Parametrisations," *Boundary-Layer Meteorology* 138, no. 3 (2011): 345–366.

16. H. Glauert, *Airplane Propellers* (Berlin, Heidelberg: Springer Berlin Heidelberg, 1935).

17. J. N. Sørensen and W. Z. Shen, "Numerical Modeling of Wind Turbine Wakes," *Journal of Fluids Engineering* 124, no. 2 (2002): 393–399.

18. P. Doubrawa, E. W. Quon, L. A. Martinez-Tossas, et al., "Multimodel Validation of Single Wakes in Neutral and Stratified Atmospheric Conditions," *Wind Energy* 23, no. 11 (2020): 2027–2055.

19. J. Berg, J. Bryant, B. LeBlanc, et al., "Scaled Wind Farm Technology Facility Overview," in *32nd ASME Wind Energy Symposium*, (National Harbor, Maryland: American Institute of Aeronautics and Astronautics, 2014), 1088.

20. P. Doubrawa, M. Debnath, P. J. Moriarty, et al., "Benchmarks for Model Validation Based on LiDAR Wake Measurements," *Journal of Physics: Conference Series* 1256, no. 1 (2019): 12024.

21. B. Kale, S. Buckingham, J. Van Beeck, and A. Cuerva-Tejero, "Implementation of a Generalized Actuator Disk Model Into WRF v4.3: A Validation Study for a Real-Scale Wind Turbine," *Renewable Energy* 197 (2022): 810–827.

22. T. Mikkelsen, N. Angelou, K. Hansen, et al., "A Spinner-Integrated Wind Lidar for Enhanced Wind Turbine Control," *Wind Energy* 16, no. 4 (2013): 625–643.

23. IEA, "IEA Wind Task 31," (2019), https://iea-wind.org/task31/.

24. N. N. Soerensen, "General Purpose Flow Solver Applied to Flow Over Hills," (1995).

25. J. A. Michelsen, "Basis3d—A Platform for Development of Multiblock PDE Solvers: - Release" (AFM 92-05. Technical University of Denmark, 1992).

26. B. Maronga, M. Gryschka, R. Heinze, et al., "The Parallelized Large-Eddy Simulation Model (PALM) Version 4.0 for Atmospheric and Oceanic Flows: Model Formulation, Recent Developments, and Future Perspectives," *Geoscientific Model Development* 8, no. 8 (2015): 2515–2551.

27. S. Domino, "Sierra Low Mach Module: Nalu Theory Manual 1.0" (SAND2015-3107W. Sandia National Laboratories Unclassified Unlimited Release (UUR), 2015), https://github.com/NaluCFD/NaluDoc.

28. M. A. Sprague, S. Ananthan, G. Vijayakumar, and M. Robinson, "ExaWind: A Multifidelity Modeling and Simulation Environment for Wind Energy," *Journal of Physics: Conference Series* 1452, no. 1 (2020): 12071.

29. W. C. Skamarock, J. B. Klemp, J. Dudhia, et al., "A Description of the Advanced Research WRF Model Version 4", NCAR/TN–556+STR (UCAR/NCAR, 2019).

30. M. Churchfield, S. Lee, P. Moriarty, et al., "A Large-Eddy Simulation of Wind-Plant Aerodynamics," in *50th AIAA Aerospace Sciences Meeting including the New Horizons Forum and Aerospace Exposition* (Nashville, Tennessee: American Institute of Aeronautics and Astronautics, 2012), 537.

31. D. K. Lilly, "On the Application of the Eddy Viscosity Concept in the Inertial Sub-Range of Turbulence," *NCAR Manuscript* 123 (1966), https://cir.nii.ac.jp/crid/1570854174475364096.

32. D. K. Lilly, "The Representation of Small-Scale Turbulence in Numerical Simulation Experiments," in *Proceedings of the IBM Scientific Computing Symposium on Environmental Science* (1967), 195–210, https://cir.nii.ac.jp/crid/1570854174114088448.

33. A. S. Monin and A. M. Obukhov, "Basic Turbulence Mixing Laws in the Atmospheric Surface Layer," *Tr. Geofiz. Inst. Akad. Nauk. SSSR* 24, no. 151 (1954): 163–187, https://cir.nii.ac.jp/crid/1573105974401174400.

34. D. Muñoz-Esparza, B. Kosović, J. Mirocha, and J. van Beeck, "Bridging the Transition From Mesoscale to Microscale Turbulence in Numerical Weather Prediction Models," *Boundary-Layer Meteorology* 153, no. 3 (2014): 409–440.

35. D. Muñoz-Esparza, B. Kosović, J. van Beeck, and J. Mirocha, "A Stochastic Perturbation Method to Generate Inflow Turbulence in Large-Eddy Simulation Models: Application to Neutrally Stratified Atmospheric Boundary Layers," *Physics of Fluids* 27, no. 3 (2015): 35102.

36. D. Muñoz-Esparza and B. Kosović, "Generation of Inflow Turbulence in Large-Eddy Simulations of Nonneutral Atmospheric Boundary Layers With the Cell Perturbation Method," *Monthly Weather Review* 146, no. 6 (2018): 1889–1909.

37. S. B. Pope, "Turbulent Flows," *Measurement Science and Technology* 12, no. 11 (2001): 2020–2021.

38. U. Högström, D. N. Asimakopoulos, H. Kambezidis, C. G. Helmis, and A. Smedman, "A Field Study of the Wake Behind a 2 MW Wind Turbine," *Atmospheric Environment (1967)* 22, no. 4 (1988): 803–820.

39. M. Magnusson and A.-S. Smedman, "Influence of Atmospheric Stability on Wind Turbine Wakes," *Wind Engineering* 18, no. 3 (1994): 139–152.

40. M. Abkar and F. Porté-Agel, "Influence of Atmospheric Stability on Wind-Turbine Wakes: A Large-Eddy Simulation Study," *Physics of Fluids* 27, no. 3 (2015): 35104.

41. J. K. Lundquist, M. J. Churchfield, S. Lee, and A. Clifton, "Quantifying Error of Lidar and Sodar Doppler Beam Swinging Measurements of Wind Turbine Wakes Using Computational Fluid Dynamics," *Atmospheric Measurement Techniques* 8, no. 2 (2015): 907–920.

42. L. Vollmer, G. Steinfeld, D. Heinemann, and M. Kühn, "Estimating the Wake Deflection Downstream of a Wind Turbine in Different Atmospheric Stabilities: An LES Study," *Wind Energy Science* 1, no. 2 (2016): 129–141.

43. C. L. Kelley and J. White, "An Update to the SWiFT V27 Reference Model" (SAND2018-11893. Sandia National Laboratories Unclassified Unlimited Release (UUR), 2018).

44. D. Tsuji, T. Boku, R. Ikeda, T. Sato, H. Tadano, and H. Kusaka, "Parallelized GPU Code of City-Level Large Eddy Simulation," in *2020 19th International Symposium on Parallel and Distributed Computing (ISPDC)* (Warsaw, Poland: IEEE, 2020), 76–83, https://ieeexplore.ieee.org/document/9201903/.

45. B. Tutkun and F. O. Edis, "A GPU Application for High-Order Compact Finite Difference Scheme," *Computers & Fluids* 55 (2012): 29–35, https://linkinghub.elsevier.com/retrieve/pii/S0045793011003227.

46. E. Elsen, P. LeGresley, and E. Darve, "Large Calculation of the Flow Over a Hypersonic Vehicle Using a GPU," *Journal of Computational Physics* 227, no. 24 (2008): 10148–10161, https://linkinghub.elsevier.com/retrieve/pii/S0021999108004476.

47. N. Janssens and J. Meyers, "Towards Real-Time Optimal Control of Wind Farms Using Large-Eddy Simulations," *Wind Energy Science* 9, no. 1 (2024): 65–95, https://wes.copernicus.org/articles/9/65/2024/.

48. M. Sanchez Gomez, J. A. Sauer, and D. Muñoz Esparza, "Supporting Data Files for "Implementation and Validation of a Generalized Actuator Disk Parameterization for Wind Turbine Simulations Within the FastEddy Model"" (Zenodo, 2024).

49. R. F. Mikkelsen, "Actuator Disc Methods Applied to Wind Turbines" (Ph.D. Thesis, Technical University of Denmark, 2004).

50. M. O. L. Hansen, *Aerodynamics of Wind Turbines*, 2nd ed. (London; Sterling, VA: Earthscan, 2008). OCLC: ocm86172940.

51. L. Prandtl and A. Betz, *Vier Abhandlungen zur Hydrodynamik und Aerodynamik: Flüssigkeit mit kleiner Reibung; Tragflügeltheorie, I. und II. Mitteilung; Schraubenpropeller mit geringstem Energieverlust* (Göttingen: Univ.-Verl, 1927).

Appendix A: Generalized Actuator (GAD) Disk Model Formulation

We implement a version of the GAD model into FastEddy to represent the effect from wind turbines on the flow. The GAD model combines one-dimensional linear and angular momentum theory (i.e., rotor disk theory) with blade-element momentum (BEM) theory to represent wind turbines as a permeable disk with a large number of blade-elements [16, 49]. One-dimensional momentum theory provides a general representation of flow immediately upstream and downstream of a wind turbine, along with the forces required to change the linear and angular momentum of the airflow. BEM theory, on the other hand, relates the aerodynamic properties of a specific wind-turbine design with the lift and drag forces imparted on the flow. Here, we provide a brief overview of the GAD model. For a more complete description of the theory, we direct the reader to R. Mikkelsen [49].

A.1 | Rotor Disk Theory

The rotor disk model is based on a rotating permeable disk (actuator disk) that slows down and adds rotation to the incoming flow [50]. The streamwise deceleration of the flow is derived from one-dimensional linear momentum theory. Rotation of the flow is estimated from one-dimensional angular momentum theory.

A.1.1 | Linear Momentum Balance

We derive an expression for the streamwise deceleration of the flow using one-dimensional momentum balance along a streamtube for inviscid, irrotational and steady flow. The mass flow rate at any given location x_i along the streamtube is given by Equation (A1), where r_{x_i} and U_{x_i} are the streamtube radius and the flow velocity at x_i, respectively, and ρ is the air density. For a streamtube that intersects the permeable disk, the mass flow $\dot{m}$ rate through the streamtube remains constant.

$$\dot{m}_{x_i} = \rho \pi r_{x_i}^2 U_{x_i} \tag{A1}$$

Because the velocity in the wake of the permeable disk is slower than far upstream, the streamtube expands downstream of the disk. As the streamtube that intersects the disk expands, the velocity in the wake U_w of the disk is slower than the velocity far upstream U_∞ by a factor $(1 - 2a_n)$, where a_n is the induction factor normal to the flow (Equation A2). Similarly, the streamwise velocity at the disk

U_n is slower than the velocity far upstream U_∞ by a factor $(1 - a_n)$ (Equation A3).

$$U_w = U_\infty(1 - 2a_n) \tag{A2}$$

$$U_n = U_\infty(1 - a_n) \tag{A3}$$

In the rotor disk model, the streamwise slowdown of the flow is caused by a force opposite to the flow (i.e., thrust force) resulting from a pressure drop at the disk location. Using Equation (A2), the thrust force T is related to the velocity far upstream as shown in Equation (A4).

$$T = \dot{m}(U_\infty - U_w) = 2\dot{m}a_n U_\infty \tag{A4}$$

A.1.2 | Angular Momentum Balance

For a wind turbine, the pressure drop across the disk is caused by blades that rotate as the air flows around them. Just as the air exerts a torque on the blades, the blades exert an equal torque on the opposite direction upon the air, causing the air to rotate in the opposite direction as the turbine. The flow starts rotating as it approaches the rotor disk. The tangential velocity U_t that forms as the flow starts rotating is related to the rotational speed of the turbine Ω and the induction factor tangential to the incoming flow a_t (Equation A5).

$$U_t = a_t \Omega r \tag{A5}$$

Assuming the wake rotation reaches half of its downstream value at the rotor disk and that the flow upstream is not rotating, the change in angular momentum of the flow that passes through the disk is caused by a torque τ given in Equation (A6).

$$\tau = \dot{m}r(\omega r) = \dot{m}r(2a_t \Omega r) \tag{A6}$$

A.2 | Blade-Element Momentum Theory

Rotor disk theory provides a simplified representation of a wind turbine that does not include turbine-specific design parameters (e.g., number of blades, airfoil characteristics). Blade-Element Momentum theory (BEM), on the other hand, provides a framework to estimate the forces imparted by the turbine on the flow that incorporates turbine-specific design characteristics. In BEM theory, a turbine rotor blade is divided into small blade elements that exert forces on the flow, which are estimated using two-dimensional aerodynamic lift and drag curves from a particular airfoil.

Lift and drag forces on each blade element are a function of the relative velocity between the blade and the flow (Figure A1). The velocity vector of the incoming flow at the turbine location is $\boldsymbol{U}_{air} = U_n\hat{\boldsymbol{n}} - U_t\hat{\boldsymbol{t}}$, where U_n and U_t are defined in Equations (A3) and (A5), respectively, and $\hat{\boldsymbol{n}}$ and $\hat{\boldsymbol{t}}$ are the normal and tangential unit vectors, respectively. The velocity of the blade element is a function of the rotational speed of the turbine and its radial location $\boldsymbol{U}_{blade} = \Omega r\hat{\boldsymbol{t}}$. The resultant relative velocity $\boldsymbol{U}_r$ between the blade element and the flow is the vector difference between $\boldsymbol{U}_{air}$ and $\boldsymbol{U}_{blade}$ (Equation A7), which acts at an angle ϕ to the plane of rotation of the disk (Equation A8). The angle of attack α in Figure A1, defined as the angle between the airfoil chord line and the resultant relative velocity, is determined by the blade twist β and the angle of the relative velocity ϕ. Wind turbine blades have a built-in twist distribution throughout the blade so that each blade element is at an angle of attack that maximizes the lift-to-drag ratio.

$$\boldsymbol{U}_r = U_\infty(1 - a_n)\hat{\boldsymbol{n}} - \Omega r(1 + a_t)\hat{\boldsymbol{t}} \tag{A7}$$

$$\phi = \arctan\frac{U_\infty(1 - a_n)}{\Omega r(1 + a_t)} \tag{A8}$$

The lift L and drag D forces for an aerodynamic element of chord length c are a function of the two-dimensional lift and drag coefficients, C_l and C_d, respectively, which are themselves functions of the airfoil angle of attack. The aerodynamic forces on a small blade element of length δr are given in Equations (A9) and (A10).

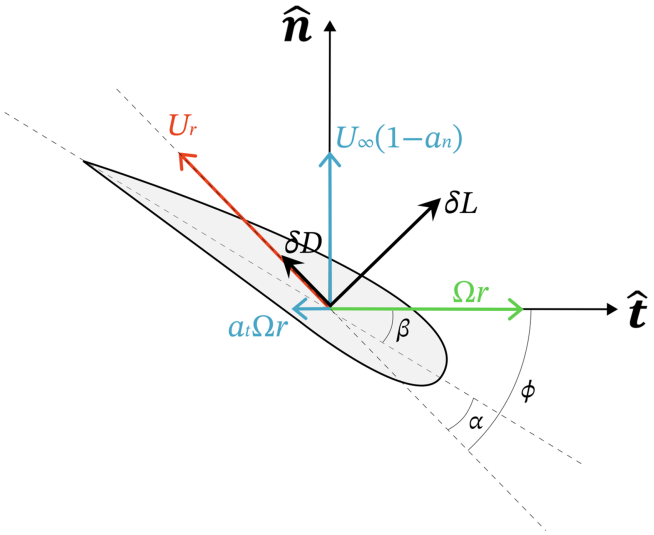

FIGURE A1 | Illustration of the velocity vectors and aerodynamic forces acting on a blade element in a normal-tangential reference frame. The velocity of the air is shown in light blue, the velocity of the blade element is shown in green, and the relative velocity between the blade and the air is shown in dark orange.

$$\delta L = \frac{1}{2}\rho c U_r^2 C_l \delta r \tag{A9}$$

$$\delta D = \frac{1}{2}\rho c U_r^2 C_d \delta r \tag{A10}$$

Projecting the lift and drag forces onto a normal-tangential coordinate system yields the thrust force (i.e., normal force) and torque-generating force (i.e, tangential force) from each blade element (Equation A11) for a turbine with B blades. Note that the solidity factor $Bc/2\pi r$ in Equations (A12) and (A13) accounts for the density of the blades in the annular disk.

$$\delta\boldsymbol{F}_{nt} = \delta F_n\hat{\boldsymbol{n}} + \delta F_t\hat{\boldsymbol{t}} \tag{A11}$$

$$\delta F_n = \frac{B}{2\pi r}(\delta L\ \cos\phi + \delta D\ \sin\phi) \tag{A12}$$

$$\delta F_t = \frac{B}{2\pi r}(\delta L\ \sin\phi - \delta D\ \cos\phi) \tag{A13}$$

A.3 | Generalized Actuator Disk Model

Rotor disk theory and BEM theory are combined to derive the forces acting on the flow. The mass flow rate for along an annular blade element δr is $\delta\dot{m} = 2\pi\rho U_n r\delta r$. Then, the thrust force (Equation A4) for each blade element can be expressed as Equation (A14). Likewise, the torque (Equation A6) acting on the flow from each blade element can be expressed as Equation (A15).

$$\delta T = 4\pi\rho r a_n(1 - a_n)U_\infty^2\delta r \tag{A14}$$

$$\delta\tau = 4\pi\rho r^3 a_t\Omega U_\infty(1 - a_n)\delta r \tag{A15}$$

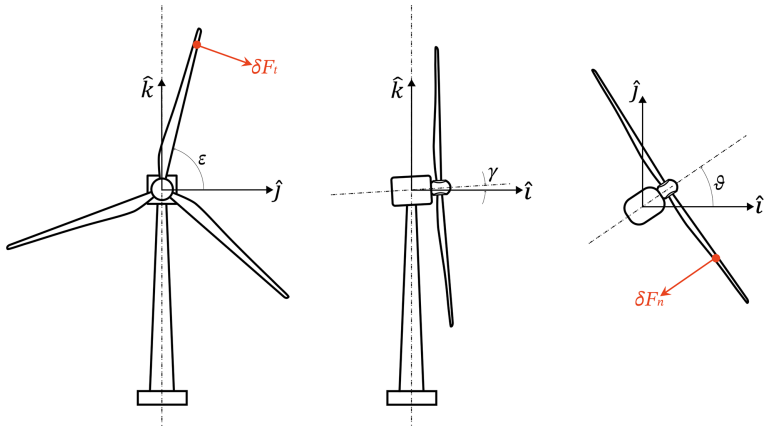

FIGURE A2 | Front-, side-, and top-view of a horizontal axis wind turbine. The azimuth angle ε, tilt angle γ, and yaw angle ϑ are shown for reference. The tangential and normal forces acting on a radial element are shown in dark orange.

Equating the thrust force derived from linear momentum theory for a blade element (Equation A14) with the normal force derived from BEM theory (Equation A12) provides an expression for the normal induction factor (Equation A16). Similarly, equating the torque derived from angular momentum theory for a blade element (Equation A15) with the torque estimated from BEM theory ($r\delta F_t$ from Equation A13) provides an expression for the tangential induction factor (Equation A17). In Equations (A16) and (A17), $\sigma = Bc/2\pi r$ is the solidity factor of the permeable annular disk and f_l is a blade tip and root loss factor.

$$a_n = \left(1 + \frac{4f_l \sin^2\phi}{\sigma(C_l \cos\phi + C_d \sin\phi)}\right)^{-1} \tag{A16}$$

$$a_t = \left(\frac{4f_l \sin\phi \cos\phi}{\sigma(C_l \cos\phi - C_d \sin\phi)} - 1\right)^{-1} \tag{A17}$$

In operational turbines, the vortices that form at the blade tip and root result in added drag that is not accounted for in the momentum analysis. At the rotor tip, flow from the high pressure side of the rotor blade passes around the blade tip to the lower pressure side forming a vortex. These vortices reduce the lift generated by the turbine close to the blade edges. Prandtl proposes a loss factor f_l that is introduced in the momentum balance in the actuator disk theory [51] (Equation A18). In Equation (A18), D is the turbine-rotor diameter and d is the diameter of the hub.

$$\begin{aligned} f_l &= f_{tip} f_{root} \\ f_{tip} &= \frac{2}{\pi}\arccos\left(e^{\frac{-B(0.5D-r)}{2r \sin\phi}}\right) \\ f_{root} &= \frac{2}{\pi}\arccos\left(e^{\frac{-B(r-0.5d)}{2r \sin\phi}}\right) \end{aligned} \tag{A18}$$

The tangential and normal forces from each blade element are projected onto the computational grid (i.e., $\hat{i},\hat{j},\hat{k}$) using successive coordinate rotations (Equation A19). The convention for each angle in Equation (A19) is illustrated in Figure A2. The tangential and normal forces are first projected onto the rotor-layer plane. Then, the forces on the rotor-layer plane are projected onto the computational grid by accounting for the turbine's rotor tilt γ ($\gamma \approx 4°$ in modern wind turbines), and yaw angle ϑ. Note that the forces acting on the flow are equal in magnitude but opposite in direction to the aerodynamic forces.

$$\begin{bmatrix} \delta F_x \\ \delta F_y \\ \delta F_z \end{bmatrix} = \begin{bmatrix} \cos\vartheta & -\sin\vartheta & 0 \\ \sin\vartheta & \cos\vartheta & 0 \\ 0 & 0 & 1 \end{bmatrix} \begin{bmatrix} \cos\gamma & 0 & \sin\gamma \\ 0 & 1 & 0 \\ -\sin\gamma & 0 & \cos\gamma \end{bmatrix} \begin{bmatrix} 1 & 0 & 0 \\ 0 & \sin\varepsilon & \cos\varepsilon \\ 0 & -\cos\varepsilon & \sin\varepsilon \end{bmatrix} \begin{bmatrix} -\delta F_n \\ \delta F_t \\ 0 \end{bmatrix} \tag{A19}$$

The forces along each coordinate are spread over multiple grid cells in the computational grid for numerical stability. We use a Gaussian regularization kernel η to distribute the forces around the turbine (Equation A20). In Equation (A20), d_n is the distance between a grid cell in the computational grid and the rotor-layer plane along the turbine's axis of rotation, and $\Delta x_{\text{eff}} = |\Delta x \cos\vartheta| + |\Delta x \sin\vartheta|$ is the grid spacing's projection onto the inflow wind vector.

$$\eta(d_n) = \frac{1}{\Delta x_{\text{eff}}\sqrt{2\pi}} e^{\left(\frac{-d_n^2}{2\Delta x_{\text{eff}}^2}\right)} \tag{A20}$$